Fluid-Structure interaction analysis and performance evaluation of a membrane blade

M. Saeedi, R. Wüchner and K.-U. Bletzinger
Technical University of Munich, Arcisstr. 21, D-80333, Munich, Germany
E-mail: mehran.saeedi@tum.de

Abstract.
Examining the potential of a membrane blade concept is the goal of the current work. In the sailwing concept the surface of the wing, or the blade in this case, is made from pre-tensioned membranes which meet at the pre-tensioned edge cable at the trailing edge. Because of the dependency between membrane deformation and applied aerodynamic load, two-way coupled fluid-structure interaction analysis is necessary for evaluation of the aerodynamic performance of such a configuration. The in-house finite element based structural solver, CARAT++, is coupled with OpenFOAM in order to tackle the multi-physics problem. The main aerodynamic characteristics of the membrane blade including lift coefficient, drag coefficient and lift to drag ratio are compared with its rigid counterpart. A single non-rotating NREL phase VI blade is studied here as a first step towards analyzing the concept for the rotating case. Compared with the rigid blade, the membrane blade has a higher slope of the lift curve. For higher angles of attack, lift and drag coefficients as well as the lift to drag ratio is higher for the membrane blade. A single non-rotating blade is studied here as a first step towards analyzing the concept for the rotating case.

1. Introduction

Various research projects have focused on flexible wings and their advantages and disadvantages compared with conventional rigid configurations. To realize a flexible wing, different concepts are used including morphing wing [1], telescopic spars [2] or using smart materials in the construction of the wing [3]. They can be grouped into two major categories: active control and passive control. In active control concepts, actuators are used to realize wing deformation, while in passive control the wing deforms due to its intrinsic flexibility. In passive control configurations, the final shape of the wing depends on the interaction between internal forces, external loading and displacement of the wing.

A membrane blade concept is studied here, which is originally an example of a passively controlled structure, whereas one could think of actuation in future realizations. Membrane structures can efficiently carry external loads over large spans via internal in-plane stresses. The response of such a blade to aerodynamic loads depends on membrane's stresses, so two-way coupled fluid-structure interaction simulations (FSI) are necessary to analyze its performance. The Sailwing research was originally initiated at Princeton University during the 1970s. In different studies, Princeton sailwing group could conclude that membrane wings have favorable characteristics compared with conventional rigid wings. From the aerodynamics point of view, membrane wings have a higher lift curve slope, a higher maximum lift coefficient and higher

lift to drag ratio compared to an equivalent rigid wing [4, 5, 6]. Delayed stall to higher angles of attack is another advantage of membrane wings [4]. From the structural dynamics point of view, membrane wings benefit from a load reduction in unsteady flow cases [7]. During the 1980s, application of the sailwing concept in wind energy systems was explored by the Princeton windmill group. The final progress report of the group states [8]: "the Sailwing rotor continues to be highly competitive in performance with its rigid-bladed counterparts and yet enjoys the benefits of simpler construction and lower costs".

Figure 1 shows the concept studied in the current work, the sailwing concept. A rigid mast forms the leading edge section of the wing. To support the upper and lower membranes, ribs are mounted along the span of the wing. Upper and lower membranes are joined together at the trailing edge via a pretensioned edge cable.

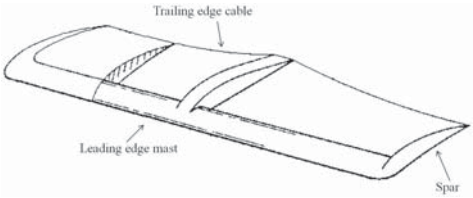

Figure 1. Sailwing construction concept, from [9]

2. Membrane Blade Concept and FSI Simulation Strategy

The proposed design workflow for the membrane blade concept is shown in figure 2. The equilibrium state of the membrane and the edge cables attached to the supporting frame is calculated in the form finding analysis. This shape represents the constructed membrane structure in the absence of external loads. Membrane and edge cable pre-stresses are the only present forces in this step. The outcome of form finding analysis presents the initial configuration of the membrane blade for the FSI analysis. The interaction between fluid flow and membrane blade is simulated during FSI analysis, followed by evaluation of the design in terms of aerodynamic characteristics like lift and drag coefficient. Depending on these characteristics the design cycle might be repeated for alternative pre-stress sets to achieve a better performance.

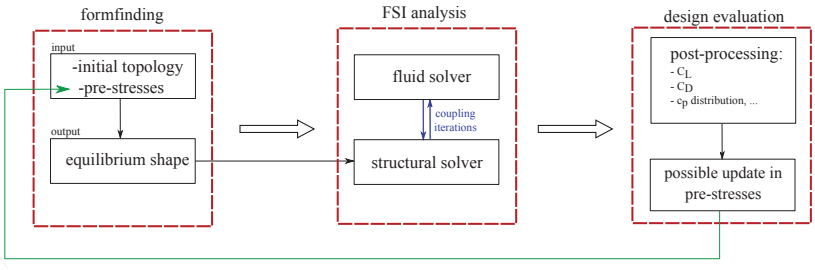

Figure 2. Design work flow

The FSI analysis is realized as a partitioned approach. OpenFOAM is used as the fluid solver and the in-house FEM solver (CARAT++) is used as the structural solver.

2.1. Fluid Model

The fluid solver, used in this work for solving the fluid flow equations is based on the *pimpleDyMFoam* solver from OpenFOAM. Large Eddy Simulation (LES) method is used for

turbulence modeling together with Spalart-Allmaras model, which is a one-equation model for calculating the kinematic eddy turbulent viscosity.

2.2. Structural Model
Structural analysis of membrane structures consists of two steps: Form Finding, which calculates the equilibrium shape of the constructed structure and static or dynamic structural analysis, which computes structure's response to external loading.

2.2.1. Form Finding Given a structure under some applied external loading, in displacement-based finite element method (FEM) displacement of the discretized structural model is calculated first, and then strain and stresses are calculated from displacements. In this context, form finding is an inverse problem, compared with structural analysis. In form finding of membrane structures, the desired stress distribution for the membrane and supporting edge cables is defined in advance for membrane elements confined to a supporting frame and edge cables. In an iterative solution procedure, form finding analysis updates the shape of the structure to a final shape, for which the prescribed stress distribution in membrane and edge cables are in equilibrium. Figure. 3 presents the example of form finding analysis for a trapezoidal membrane. The membrane is fixed at the horizontal and vertical edges, while it is supported by a pre-stressed cable at the inclined edge. Two pre-stress sets are presented for the membrane pre-stress in the vertical and horizontal direction (σ_V, σ_H) and cable pre-stress (σ_C). As it can be seen, when cable pre-stress is higher than membrane pre-stress, it can "resist" the tensile force from the membrane and undergoes smaller deformation. Whereas for the case of equal pre-stresses the membrane force is strong enough to pull the initially straight edge cable into a curved configuration. Different methods are used in form finding analysis, including the force density

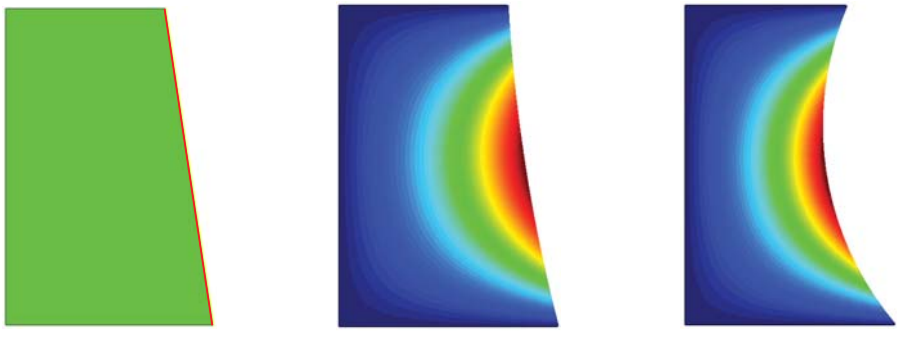

Figure 3. Form finding of a trapezoidal membrane. Initial configuration (left), $\sigma_H = \sigma_V, \sigma_C = 8\sigma_V$ (middle), $\sigma_H = \sigma_V = \sigma_C$ (right)

method, dynamic relaxation and the updated reference strategy (URS). The URS method is utilized in the current work, for details on the method we refer to [10].

2.2.2. Dynamic Analysis The equation governing the dynamic behavior of the system reads:

$$\mathbf{M}\ddot{\mathbf{x}} + \mathbf{C}\dot{\mathbf{x}} + \mathbf{K}\mathbf{x} = \mathbf{f}, \tag{1}$$

where $\mathbf{M}$, $\mathbf{C}$ and $\mathbf{K}$ are respectively the mass, damping and stiffness matrices and $\mathbf{f}$ is the applied external loading. Rayleigh damping, which estimates the damping matrix as a linear

combination of the mass and stiffness matrices is used:

$$\mathbf{C} = \alpha\mathbf{M} + \beta\mathbf{K}. \tag{2}$$

Newmark's β method is used for time integration. The method uses a linear combination of the acceleration at the current time step and the next time step to calculate the velocity and consequently the displacement for the new time step:

$$\dot{\mathbf{x}}_{n+1} = \dot{\mathbf{x}}_n + (1-\gamma)\ddot{\mathbf{x}}_n\Delta t + \gamma\ddot{\mathbf{x}}_{n+1}, \tag{3}$$

and

$$\mathbf{x}_{n+1} = \mathbf{x}_n + \dot{\mathbf{x}}_n\Delta t + (\frac{1}{2} - \beta)\ddot{\mathbf{x}}_n\Delta t^2 + \beta\ddot{\mathbf{x}}_{n+1}\Delta t, \tag{4}$$

where γ and β are model constants. First $\ddot{\mathbf{x}}_{n+1}$ is calculated in terms of the known parameter (the parameters from the current time step) and $\mathbf{x}_{n+1}$ using equation 4. The calculated $\ddot{\mathbf{x}}_{n+1}$ is then inserted in equation 3 in order to calculate $\dot{\mathbf{x}}_{n+1}$. Inserting both $\ddot{\mathbf{x}}_{n+1}$ and $\dot{\mathbf{x}}_{n+1}$ into equation 1 and after necessary rearrangements we have:

$$\mathbf{K}^*\mathbf{x}_{n+1} = \mathbf{f}^*_{n+1}, \tag{5}$$

where $\mathbf{K}^*$ is the effective stiffness matrix and $\mathbf{f}^*$ is the effective external load vector, both calculated in terms of displacement, velocity and acceleration of the current time step.

2.3. Fluid-Structure Interaction

A partitioned approach is utilized for realizing the solution of the coupled problem. The partitioned approach enables the development of a modular FSI toolchain, where the two fields could be solved separately using the most efficient techniques available for each field problem. An in-house coupling tool is used to link the fluid solver with the structural solver and manage the data exchange between the two solvers. The coupling condition between the two fields is enforced at the interface. The coupling conditions include kinematic continuity condition, which guarantees that the fluid and structure interface lie on each other during the simulation and dynamic continuity condition, which takes care of conservation of the tractions which are mapped from the fluid interface to structure interface.

Mortar mapping is used for mapping of structural displacement and nodal forces between the two solvers. It is consistent, i.e. a constant field is mapped exactly from one mesh to the target mesh. The mapping should be done in a conservative manner, meaning that the total energy should not change as the field is mapped between the interface meshes:

$$\int_{\Gamma^F} \mathbf{d}_\Gamma^{F^T}\mathbf{f}_\Gamma^F d\Gamma^F = \int_{\Gamma^S} \mathbf{d}_\Gamma^{S^T}\mathbf{f}_\Gamma^S d\Gamma^S, \tag{6}$$

where Γ^F and Γ^S designate respectively the fluid and the structure interface. Mortar mapping is not consistent in general. A novel technique for enforcing consistency on Mortar mapping is used, where consistency is realized by scaling of the structural shape functions for calculating the mapping matrices [11].

A generic coupling iteration follows these basic steps:

(i) Solve the fluid problem for time step n
(ii) Send the resulting force at the interface to the structure solver
(iii) Solve the structure problem
(iv) Send the calculated displacement to the fluid solver and proceed to the next time step (or next iteration)

In implicit coupling, the iterations are done for multiple times within each time step to improve stability and accuracy of the solution. Schematic presentation of implicit coupling scheme is shown in figure 4.

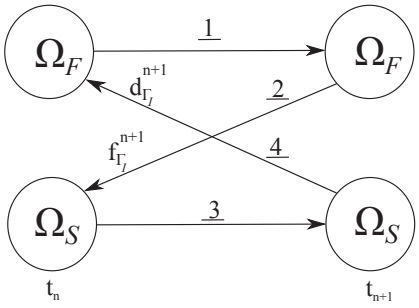

Figure 4. Implicit coupling scheme

3. Model Setup and Results

The studied membrane blade can be seen in figure 5. It is the NREL phase VI blade with the length of 5.029 m. Upper and lower membranes are wrapped around the rigid leading edge which extends up to 15% of the chord length. From the section where the upper and lower membranes are attached to the rigid transition region to the tip of the blade, the membranes are supported by 4 flexible ribs and by an edge cable at the trailing edge. The 4 ribs divide the blade into 4 segments with equal spans. An important point in the conceptual design of the membrane blade is the decision on the number of segments for a given blade. With the increase in the span of an individual segment (higher aspect ratio), the shrinkage of the membranes during the form finding analysis increases. To avoid this, a larger span-wise to chord-wise pre-stress ratio is necessary in order to get a reasonable equilibrium shape for segments with higher aspect ratio. This can be realized either by increasing the span-wise pre-stress or by decreasing the pre-stress in the chord-wise direction. Since changing the chord-wise pre-stress requires adaptation the trailing edge cable pre-stress as well, adjusting the span-wise pre-stress is the better choice for getting a reasonable equilibrium shape. There is a trade-off between increasing the span-wise pre-stress for segments with higher aspect ratio and the decrease in membrane's flexibility with the increase of the pre-stress level. From the experience, it is very difficult to find a proper set of pre-stresses for segment aspect ratios higher than 3. At the current set-up, the aspect ratio of the individual segments increases from 1.37 to 2.34 from the root segment to the tip segment.

3.1. Form Finding

Structural properties of the membranes, ribs (modeled as beams) and edge cable are summarized in tables 1 to 3. The pre-stresses in table 1 are for the first blade section from the root. The pre-stress in span direction is the same for all 4 segments since they all have the same span, but the pre-stress in chord direction is scaled with the mean chord length for the three other segments.

After the transition region from the cylindrical part of the blade, the cross section of the blade is the S809 airfoil profile. During the form finding analysis the blade shrinks, the upper membranes move downward and the lower membranes move upward. The cross section does not change at the ribs. Apart from the 4 ribs the blade has a varying cross section as it is shown in figure 6. The deformed configuration, presented in the picture is the outcome of the form finding analysis. This configuration represents the shape at which membrane pre-stresses and edge cable pre-stresses are in equilibrium. It is the shape of the constructed blade in the absence of any external loading and consequently serves as the initial configuration for FSI analysis.

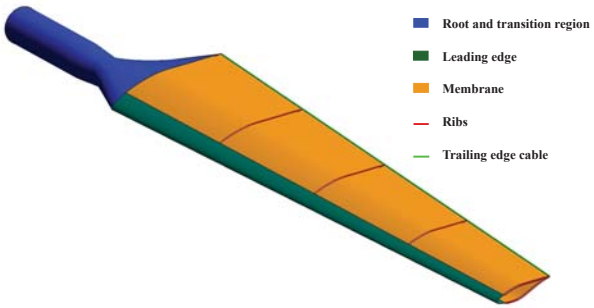

Figure 5. Blade planform

Table 1. Membrane properties, (u: upper, l: lower)

E	$84MPa$
ρ	$1400kg/m^3$
t	$0.48mm$
$\sigma^u_{chordwise}$	$180kPa$
$\sigma^u_{spanwise}$	$480kPa$
$\sigma^l_{chordwise}$	$180kPa$
$\sigma^l_{spanwise}$	$480kPa$

Table 2. Trailing edge cable properties

E	$125GPa$
ρ	$7800kg/m^3$
$radius$	$4mm$
σ	$30MPa$

Table 3. Rib properties

E	$190GPa$
ρ	$7800kg/m^3$
A	$2cm \times 12cm$

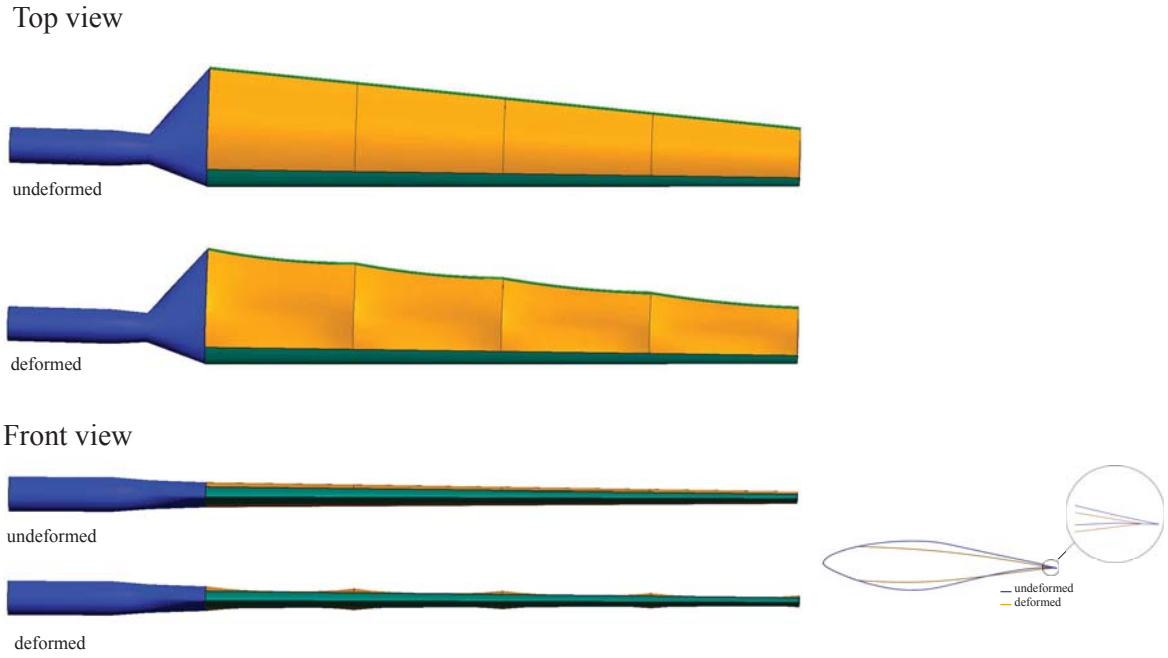

Figure 6. Form finding analysis, deformed and undeformed configuration for the blade's top and front view and cross section at the middle of the second segment from the root

3.2. Fluid Setup

For solving the fluid problem pimpleDyMFoam solver was used with slight modification for managing the data exchange between the fluid and the structural solver. The computational domain together with its discretization near the blade is presented in figure 7. The domain size is $15m \times 15m \times 45m$, which results in a blockage ratio of about 0.3%. The root of the blade is attached to one of the side walls, while the tip of the blade has a distance of 10m to the other side wall which forms the far field boundary. The two side walls are modeled as slip walls. The simulations are done for a uniform far-field velocity of 30m/s. The fluid domain is discretized into 2.9 million elements, which results in a y^+ value of approximately 70 for blades surface. There are 90 cells in chord direction on the pressure side as well as on the suction side of the blade. In the spanwise direction, 49 layers of elements are used for discretization of the blade.

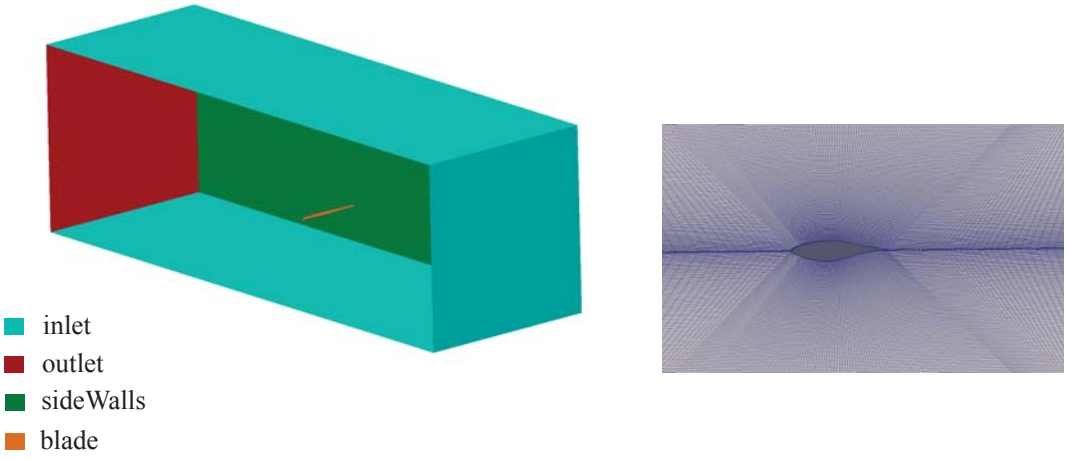

Figure 7. Fluid Domain (left), fluid mesh in the vicinity of the blade (right)

3.3. FSI Analysis

The coupled problem of the interaction between membrane deformation and external fluid flow is solved for a total of 6 seconds with a time step size of 0.001 seconds. In order to improve the stability, the calculated displacement at each iteration is relaxed by a factor (ω_r) between 0.1 and 0.3 (depending on the angle of attack) before being sent to the fluid solver:

$$\mathbf{d}^{n+1}_{\Gamma_{I,sent}} = \omega_r \mathbf{d}^{n+1}_{\Gamma_{I,calculated}} + (1-\omega_r)\mathbf{d}^{n}_{\Gamma_I} \tag{7}$$

Applying the relaxation factor helps to preserve the quality of the fluid mesh as it deforms during FSI simulation. Simulation results are presented in the sequel.

Blade Profile Comparison As a result of the applied aerodynamic load, the membrane on the upper side of the blade moves upward and on the lower side, depending on the angle of attack, the membrane moves either downward or upward. Blade's cross section at the ribs remains unchanged (S809 profile), but apart from the ribs the cross section changes along the blade. Comparison of the mean cross section profile with the undeformed cross section and the S809 profile is made in figure 8 for the mid-span section of the second segment from the root. The undeformed profile at the figure represents the cross section at the beginning of the FSI simulation ($t = 0sec$), which is the shape calculated during the form finding analysis. the deformed shape at the end of form finding analysis is the undeformed shape for the FSI simulations.

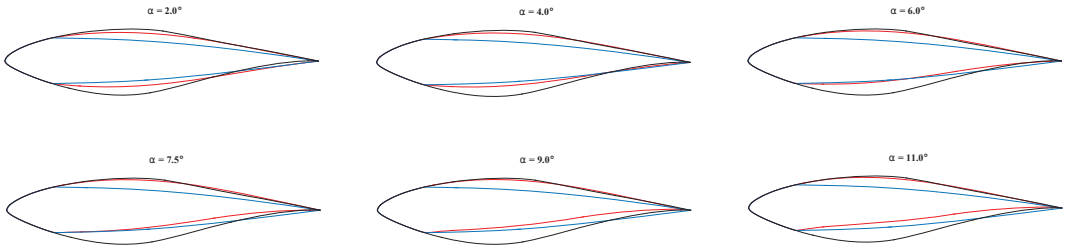

Figure 8. Blade's cross section comparison: S809 profile (black), undeformed profile (blue) and deformed profile (red).

Displacement over Time Displacement of the membrane at a selected monitor point on the upper membrane which is located at $x/c = 0.5$ position on the mid-span cross section for the second segment from the root is presented in Fig. 9. For the seven studied angles of attack oscillations in the membrane are damped out with time for all except $\alpha = 11.0°$. For this case, displacement at the monitor point oscillates around a mean value of $0.0181m$ with a standard deviation of 2.54×10^{-5}. As it can be seen in the figure for $\alpha = 0.0°$ to $\alpha = 9.0°$, displacement is increasing with angle of attack but from $\alpha = 9.0°$ to $\alpha = 11.0°$ there is a decrease in the displacement. Taking acting forces on the blade into account, it is not the lift force which dominates the displacement of the membrane, there exists a correlation between the displacement of the monitor point and lift to drag ratio (figure 10).

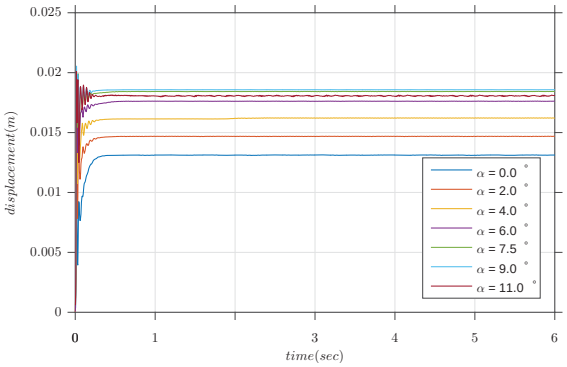

Figure 9. Membrane displacement at the monitor point

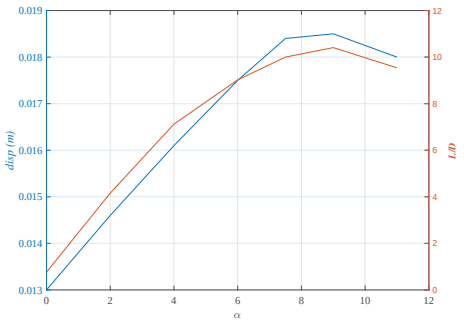

Figure 10. Correlation between membrane displacement and L/D

Camber Line The camber of the blade changes as a result of membrane's deflection. The S809 airfoil of the rigid blade has a maximum camber of about 1% located at 82.3% chord position. At the unloaded condition the membrane wing has a rather symmetric profile (excluding rib sections and their neighborhood). Under the action of the applied aerodynamic load, maximum camber increases with angle of attack, and as shown in figure 11 the point of maximum camber shifts toward the leading edge. Starting from $\alpha = 4.0°$ the membrane blade has higher camber compared with its rigid counterpart.

Aerodynamic Coefficients Because of vortex shedding at the cylindrical part of the blade and also because of flow separation at higher angles of attack ($\alpha = 9.0°$ and $\alpha = 11.0°$) and slight oscillations in the membrane, the force acting on the membrane blade have also an oscillatory

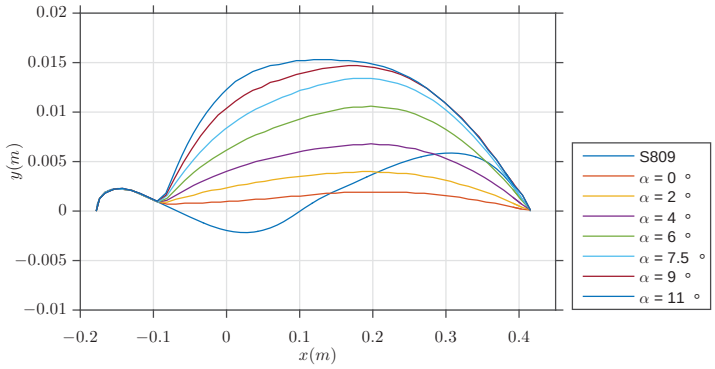

Figure 11. Camber line at the mid-span section for the second segment form blade's root

Table 4. Maximum camber and its location for the membrane blade

$\alpha(deg)$	0.0	2.0	4.0	6.0	7.5	9.0	11.0
Max Camber (%)	0.38	0.67	1.14	1.78	2.26	2.52	2.63
Location of Max Camber	65.2	63.2	63.2	63.2	61.2	60.0	52.0

behavior (figure 12). Spectral analysis of the lift coefficient is presented in figure 13, the two dominant frequencies correspond to vortex shedding at the root section of the blade and flow separation over the blade.

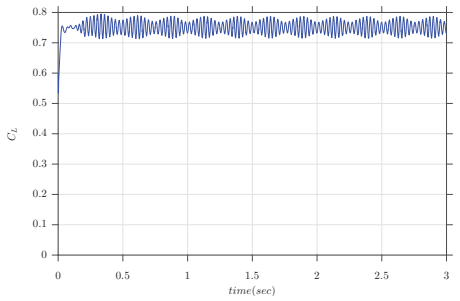

Figure 12. lift coefficient for the membrane blade, $\alpha = 9.0°$

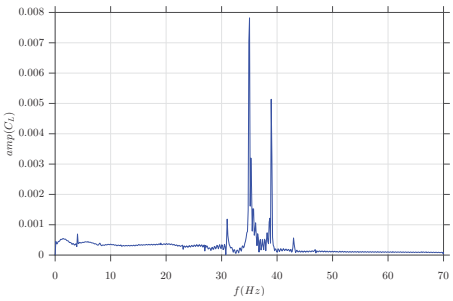

Figure 13. Spectral analysis of the lift coefficient, $\alpha = 9.0°$

Membrane vibrations change the spectral response of the loading on the blade which is of utmost importance in fatigue analysis of the blade. The comparison between the spectra of the lift coefficient between the membrane blade and the rigid blade is shown in figure 14. There is a shift toward the right for the dominant frequency of the membrane wing, furthermore, the amplitude of the oscillation in the lift coefficient at the dominant frequencies is less for the membrane blade, which can be an advantage over the rigid blade in the context of fatigue analysis.

Comparison of lift coefficient, drag coefficient and the lift to drag ratio between the membrane blade and its rigid counterpart is made in figures 15 to 17. Since the unloaded membrane blade has a rather symmetric profile, at $\alpha = 0.0°$ the membrane blade has a smaller lift coefficient compared with the rigid blade with the asymmetric S809 airfoil. With the increase of angle of

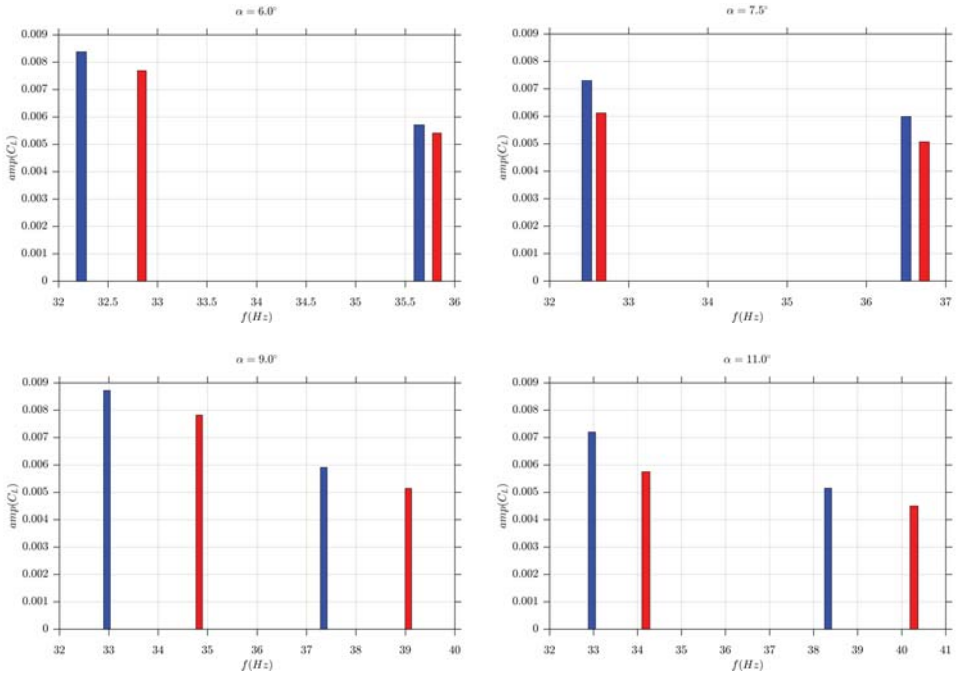

Figure 14. Change of the dominant frequencies for the membrane wing (red) compared with the rigid wing (blue).

attack the camber, and consequently the lift coefficient, increases for the membrane blade. Even though the zero angle of attack lift coefficient is smaller for the membrane blade, the slope of the lift curve is higher for the membrane blade and starting from $\alpha \approx 4.5^\circ$ the lift coefficient is higher for the membrane blade.

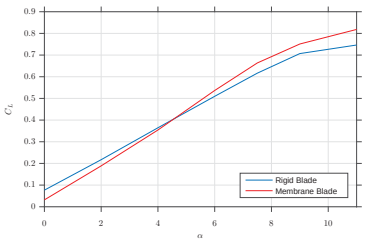

Figure 15. Lift coefficient comparison

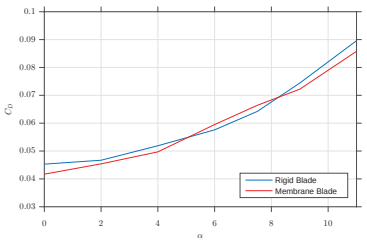

Figure 16. Drag coefficient comparison

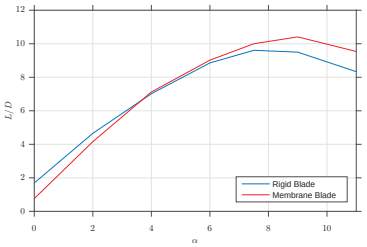

Figure 17. Lift to drag ratio comparison

Quantitative comparison of lift coefficient, drag coefficient and the lift to drag ratio is summarized in table 5.

Pressure Distribution Comparison Improvement of the lift coefficient for the membrane blade over its rigid counterpart can also be seen in the pressure distribution over the blade. The comparison is made in figure 18 for the pressure coefficient at the mid-span section for the second segment from the root. The kink in the pressure coefficient distribution for the membrane blade

Table 5. Percentage change in aerodynamic coefficients of the membrane blade compared with the rigid blade

$\alpha(deg)$	0.0	2.0	4.0	6.0	7.5	9.0	11.0
Δc_L	-58.54	-13.12	-2.83	5.28	7.64	6.25	9.63
Δc_D	-7.95	-2.78	-4.24	3.30	3.43	-2.96	-4.24
$\Delta(L/D)$	-54.94	-10.66	1.48	1.86	4.08	9.58	14.46

is due to discontinuity in surface slope at the point where the membrane is attached to the rigid leading edge.

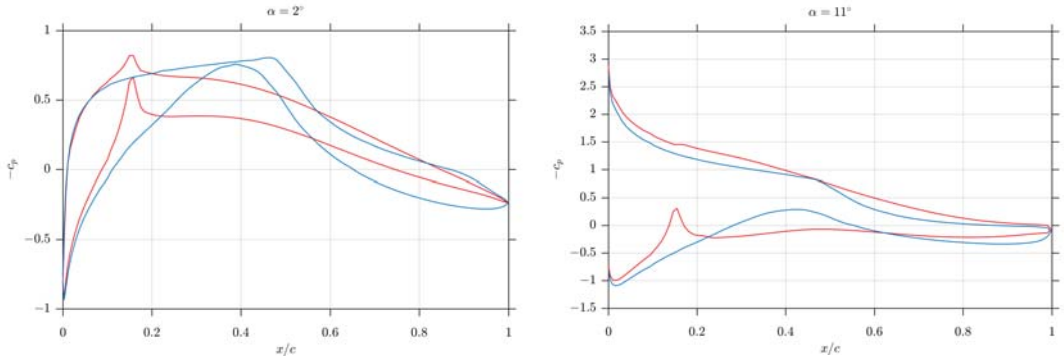

Figure 18. Pressure distribution comparison, rigid blade (blue), membrane blade (red)

4. Conclusion

Unsteady fluid-structure interaction analysis of a membrane blade concept is done for the non-rotating configuration in a partitioned simulation environment using OpenFOAM as the fluid solver and an in-house FEM based structural solver. The aerodynamic performance of the membrane blade in terms of the lift and drag coefficient and the lift to drag ratio is compared with its rigid counterpart. Further high-fidelity simulations need to be performed for mode detailed analysis of the membrane blade concept.

The lift coefficient at zero angle of attack is smaller for the membrane blade, but due to the higher lift curve slope the membrane blade demonstrates higher lift coefficient and lift to drag ratio for higher angles of attack compared with the rigid blade. An increase of camber with angle of attack and also shifting of the point of maximum angle toward the leading edge is observed for the membrane blade. The maximum lift to drag ratio is also larger for the membrane blade. These results together with lighter construction of the membrane blade promise the potential of this concept for wind turbines. Structural response and aerodynamic performance of the rotating blade for unsteady inflow condition should also be studied before making further conclusions.

Acknowledgement

The financial support provided by the Deutsche Forschungsgemeinschaft (DFG) (BL 306/32-1) is gratefully acknowledged.

References

[1] Bowmann, J., Sanders, B., Cannon, B., Kudva, J, Joshi, S., Weisshaar, T., "Development of Next Generation Morphing Aircraft Structures,"AIAA Conference, Honolulu, Hawaii, April 2007. doi:10.2514/6.2007-1730
[2] Blondeau, J., Richeson, J., and Pines, J.D., "Desing, development and testing of a morphing aspect ratio wing using an inflatable telescopic spar," AIAA Conference, 2003. doi:10.2514/6.2003-1718
[3] Barbarino, S., Dettmer W., Friswell M.: Morphing Trailing Edges with Shape Memory Alloy Rods, ICAST 2010
[4] Maughmer M.D., "A Comparison of the Aerodynamic Characteristics of Eight Sailwing Airfoil Sections," Proceedings of the 3rd International Symposium on the Science and Technology of Low Speed and Motorless Flight, Hampton, VA, USA, 29-30 March 1979, pp. 155-176.
[5] Fink M., "Full-scale Investigation of the Aerodynamic Characteristics of a Sailwing of Aspect Ratio 5.9," NASA-TN-D-5047, February 1969.
[6] Saeedi M., Wüchenr R., Bletzinger K.-U, "Multi-fidelity Fluid-Structure Interaction Analysis of a Membrane Wing," 17th International Conference on Applied Aerodynamics and Aeromechanics, London, 2015.
[7] Levin, O., Shyy, W., "Optimization of a flexible low Reynolds number airfoil," 39th Aerospace Sciences Meeting and Exhibit, Aerospace Sciences Meetings, January 2001. doi:10.2514/6.2001-125
[8] Maughmer M.D., "Optimization and Characteristics of a Sailwing Windmill Rotor," Princeton University, March 1976
[9] Ormiston R., "Theoretical and Experimental Aerodynamics of the Sailwing," Journal of Aircraft, Vol. 8, No. 2, 1971, pp. 77-84. doi: 10.2514/3.44232
[10] Wüchner, R., and Bletzinger, K.-U., "Stress-adapted numerical form finding of pre-stressed surfaces by the updated reference strategy," Intertaional Journal for Numerical Methods in Engineering, Vol. 64, No. 2, September 2005, pp. 143-166. doi: 10.1002/nme.1344
[11] Wang T., Wüchner R., Sicklinger S., Bletzinger K.-U.: Assessment and improvement of mapping algorithms for non-matching meshes and geometries in computational FSI, J. Computational Mechanics, doi=10.1007/s00466-016-1262-6, 2016.